

Coseismic DInSAR Analysis of the 2020 Petrinja Earthquake Sequence

Bálint Magyar^{1,2*}

¹ Lechner Nonprofit Ltd. - Satellite Geodetic Observatory, Budafoki út 59., H-1111 Budapest, Hungary

² Department of Geodesy and Surveying, Faculty of Civil Engineering, Budapest University of Technology and Economics, Műgyetem rkp. 3., H-1111 Budapest, Hungary

* Corresponding author, e-mail: balint.magyar@lechnerkozpont.hu

Received: 09 December 2021, Accepted: 09 April 2022, Published online: 10 June 2022

Abstract

Interferometric SAR analysis provides an excellent opportunity to perform large-scale and rapid coseismic deformation mapping. Between December 28–30, 2020, three earthquakes with magnitudes greater than 4.3 occurred during the 2020 Petrinja Earthquake Sequence near Petrinja in Croatia, resulting in significant coseismic deformation. Considering both the available ascending and descending Sentinel-1A/B images preceding and following the Petrinja Earthquake Sequence, 2.5D differential interferometric analysis was performed to determine the resulting deformation field, which have significant importance in civil engineering related countermeasures and hazard assessment. With the applied methodology, the derived horizontal and vertical deformation fields can be characterized by a maximum of ± 0.43 m local East-West, a maximum of 0.15 m local subsidence and a maximum of 0.19 m local vertical uplift near Petrinja.

Keywords

Sentinel-1, 2.5D DInSAR, Petrinja, coseismic deformation

1 Introduction

Several significant and three, greater than 4.8 magnitude earthquakes occurred near Petrinja in Sisacko-Moslavacka Zupanija, Croatia, between December 28 and December 30, 2020 (Fig. 1). As the foreshock, the M5.3 oblique fault derived earthquake occurred at a relatively shallow depth of 10 km, with an epicenter ~ 8 km west of Petrinja at 05:28:08 (UTC) December 28, 2020. The following M6.4 mainshock occurred the following day at 11:19:54 (UTC) with the epicenter ~ 3 km west-southwest of Petrinja at a depth of 10 km, driven by strike-slip faulting. The M4.8 aftershock occurred at 05:15:04 (UTC), ~ 9 km west of Petrinja at a shallow 5.4 km depth. The earthquakes can be generally characterized as intraplate earthquakes of the Eurasia plate due to their shallow depths, where the origin of the recent tectonic stress corresponds to the kinematics of the Adria microplate, namely its counter-clockwise rotation and north-northeastern motion relative to Eurasia [1–7]. The epicenters and the corresponding United State Geological Survey (USGS) focal mechanism solutions (FMS) [8] are illustrated in Fig. 1. with the indicated area of interest. According to the introduced data on the Petrinja

earthquake sequence, strong coseismic deformation can be assumed. Coseismic deformations can significantly affect the anthropogenic environment and infrastructure, as well as the natural surface [9–12]. The consequences of the Petrinja earthquake sequence were severe, both in terms of fatalities and economic loss. The evaluation of the coseismic deformation field is required to increase the

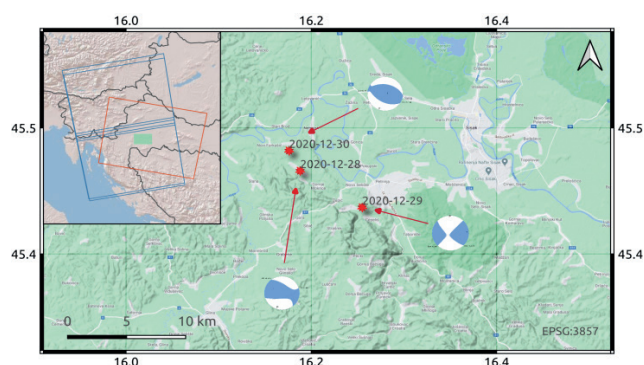


Fig. 1 Area of interest and indication of epicenters and FMS of the 2020.12.28–30 Petrinja Earthquake sequence. The overview plot indicates the marked area of interest and the footprints of the Sentinel-1 Level-1 input data (blue: ascending, red: descending tracks)

understanding of continental lithosphere behavior, as well as to enhance further scientific research and hazard assessment [9]. For obtaining data on such a deformation field, Synthetic Aperture Radar (SAR) Interferometry, InSAR, has become a widely used remote sensing and geodetic method [9, 13]. To obtain the coseismic deformation field of Petrinja earthquake sequence, differential interferometric SAR (DInSAR) processing was performed.

2 Methodology

Interferometric synthetic aperture radar (InSAR) is one of the fastest developing remote sensing techniques. The physical characteristics of the acquisition modes make weather and daytime independent Earth observation possible. The technology utilizes the phase information of complex synthetic aperture radar (SAR) images taken over a period of time. In case of surface deformation, relative phase differences occur between two acquisition times, which may be converted to satellite line-of-sight (LOS) deformation. The concept of the applied Differential-InSAR (DInSAR) analysis, the respective acquisition and orbit geometry are summarized in Fig. 2. below.

Conducting the DInSAR analysis, a classical 2-pass differential interferometry was performed, namely with an InSAR pair and a simulated interferogram based on an existing Digital Elevation Model (DEM) [14] for each

ascending and descending track. DInSAR processing aims at the separation of the topographic and the displacement terms of the interferograms, by removing the topography related phase components. The 2-pass differential interferometry was performed with the GAMMA Software package [15].

The main input of the DInSAR analysis were interferometric wide swath mode of Sentinel-1A (S1A) and Sentinel-1B (S1B) TOPS (Terrain Observation with Progressive Scanning) level-1 [16, 17] acquisitions. These Single Look Complex (SLC) [16, 17] datasets with VV polarization have been utilized and accessed via the Alaska Satellite Facility [18]. For the Petrinja earthquake sequence, a proper selection of master and slave images have been performed in ascending relative orbit number of 146 (A146), and descending relative orbit number of 124 (D124) summarized in Appendix 1. The formed interferometric pairs of 20201224-20201230 for the A146 and 20201223-20210104 for D124 assures that both master acquisitions precede the M5.3 foreshock, as well as that the corresponding slave acquisitions are subsequent to the M4.8 aftershock. Taking advantage of the 6-day revisiting time of the Sentinel-1 mission, coseismic deformation mapping can be performed with short temporal baselines of 6 days and 12 days. Footprints of the input data are presented in the overview plot of Fig. 1.

Additionally, auxiliary input data can be specified, namely the POD (Precise Orbit Determination) Restituted Orbit state vectors of the Sentinel-1 mission, provided by Sentinel-1 Quality Control (S1QC) [19]. The validity dates of the utilized restituted orbit vectors correspond to the acquisition dates of the SLCs. Conventionally, interferometric analyses apply precise orbit ephemerides or equally precise orbit data, with a position accuracy of 5 cm with 3D 1-sigma RMS, for evaluating precise orbit state vectors and corresponding baselines for the interferometric pairs. Although such precise orbit ephemerides products of S1QC are only available 20 days after the acquisition date, restituted orbit state vectors with 10 cm position accuracy and 2D 1-sigma RMS are available within 3 hours after the acquisition; thus, delivering DInSAR results with such S1QC orbit state vectors is a good compromise [15, 19–20]. After initializing the input data, noise calibration was carried out. The resulting SLC images have been mosaiced from TOPS mode [17] and multi-looked with a factor of 10 in range and with factor of 2 in azimuth, to reduce the speckling effect and obtain approximately square pixels in the multi-look intensity (MLI)

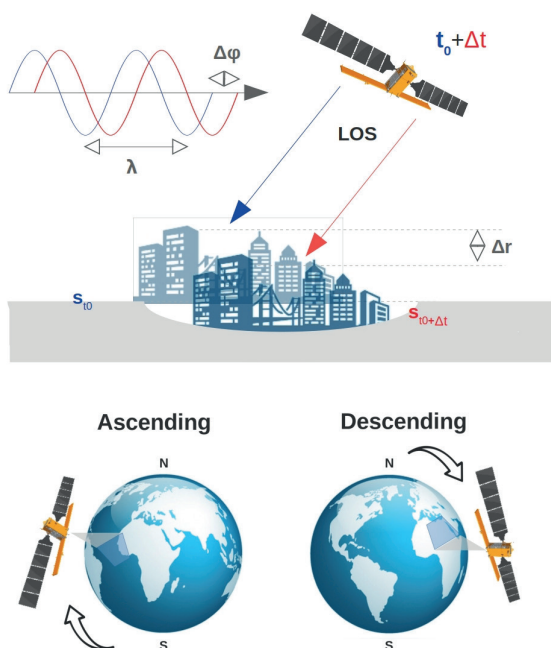


Fig. 2 Top panel: 2-pass DInSAR basics (initial acquisition time: t_0 , subsequent acquisition time: Δt , LOS: line-of-sight direction, undeformed surface: s_0 , deformed surface $s_0 + \Delta t$, $\Delta\phi$: relative phase difference). Bottom panel: visualization of the ASC/DESC orbits

images with ~ 25 by 25 m ground pixel size. According to the 2-pass DINSAR approach, the initial DEM [14] must be transformed to radar geometry in order to compute and subtract the topographic phase. In order to achieve transformation between radar and DEM geometry, lookup table and intensity cross-correlation computation were performed as described in [21]. This process includes the calculation of an initial lookup table between the geodetic coordinates of the DEM and the radar-doppler coordinates (RDC) of the SAR data, as well as the simulation of the SAR intensity image using DEM-topography and its iterative fine registration and lookup table refinement via polynomial offset tracking [21]. With the refined lookup-table, resampling of the DEM to RDC can be achieved as forward geocoding, while backward geocoding can be performed to resample data in the SAR geometry to the geodetic coordinate system [15].

As the next step of the of the DInSAR processing, co-registration with sub-pixel accuracy (~ 0.0001 pixel in azimuth direction) of the SLC images was achieved. The co-registration of TOPS mode A146 and D124 interferometric pairs was performed as an iterative improvement of master-slave spatial resampling with fine image registration, using the enhanced spectral diversity method as well as cross-correlation based intensity matching [15, 22]. The final co-registration accuracy was -0.000390 azimuth pixels for the A146 interferometric pair, and -0.000074 azimuth pixels for the D124 interferometric pair. On the co-registered SLC pairs, azimuth phase ramp caused by the Doppler-Centroid variation was also calculated and subtracted from the co-registered and resampled TOPS SLC data. After the co-registration and deramping process, according to the area of interest (AOI) indicated in Fig. 1, a subset selection of the initial TOPS data was executed, where the SLC data follows Doppler-Centroid range phase convention [15].

To perform 2-pass differential interferometry aiming to specify the corresponding line-of-sight (LOS) deformation fields for both ascending and descending tracks, simulation of the unwrapped interferometric phase is required. This is carried out by simulating the unwrapped and unflattened phase components of the corresponding topography (DEM), the orbit state vectors, the derived baselines, and the curved Earth phase-trends [9, 13, 15]. Prior to forming the complex interferogram, common-band filtering is performed on the co-registered master and slave SLCs. From the co-registered and range-adaptive common-band filtered SLC images the complex normalized interferogram can be computed with cross-correlation [15].

As the object of the 2-pass differential interferometry, the resulting complex differential interferogram can be derived by subtracting the simulated unwrapped phase, which contains the topographic phase from a complex normalized interferogram. To obtain complex differential interferogram with reduced phase noise, local-fringe spectrum based adaptive filtering was also performed [23]. The resulting multi-looked and filtered complex differential interferogram are illustrated after backward geocoding in Fig. 3, for both A146 and D124 orbit tracks.

As Fig. 3 illustrates, the coseismic differential interferogram clearly indicates the rupture zone along the strike-slip fault, which is significantly affected by decorrelation and phase noise. Since the interferometric phase is only known modulo 2π from the derived complex interferogram, a phase unwrapping step needs to be performed to retrieve deformation related information, by adding the proper multiple of 2π . Similar to the GNSS phase ambiguity problem [24–25], to solve the phase unwrapping problem, global optimization technique of Minimum Cost Flow (MCF) with successive shortest path (SSP) realization method was performed on an irregular triangular mesh [26–29]. Enhancing the robustness of the phase unwrapping, the interferometric coherence was used as weights for MCF unwrapping [27, 29].

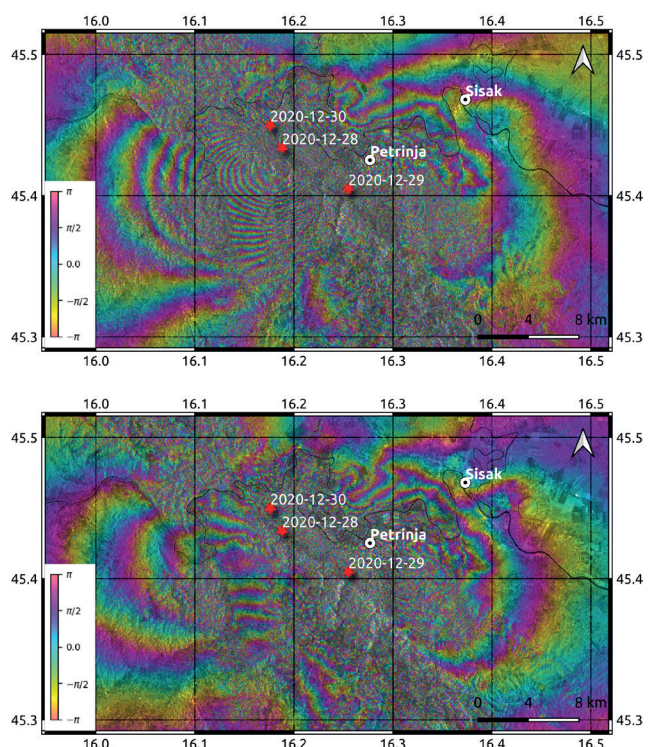


Fig. 3 Co-seismic normalized complex differential interferograms of the 2020.12.28–30 Petrinja Earthquake sequence. Top panel corresponds to ascending, bottom panel corresponds to descending solution

Subsequently, the next step, namely deriving Line-of-sight (LOS) displacements (Fig. 4) can be evaluated via scaling the unwrapped differential phase [29], using:

$$\Delta\rho = \frac{\lambda}{4\pi} \phi_u, \quad (1)$$

where ϕ_u corresponds to the unwrapped differential phase, λ to the wavelength of the C-band SAR instrument that acquired the SLC data, while $\Delta\rho$ corresponds to changes of distance from the radar to the ground target expressed in meters (LOS deformation). The accuracy of such measurements are discussed in [13].

LOS deformation is considered negative if the displacement occurred away from the SAR sensor (Fig. 4, colormap: red) [29–30]. Results indicate negative LOS deformations near Petrinja and along the surrounding valley of the Kupa River in the ascending solution (Fig. 4, top panel), while negative LOS displacements for the descending solution can be identified near the valley and estuary of the Glina River (Glinksa Poljana and Slana) in the bottom panel of Fig. 4. Corresponding positive LOS displacements, namely deformations where motion occurs towards the satellite (Fig. 4, colormap: blue) were identified in Petrinja according to the descending solution (Fig. 4, bottom panel), as

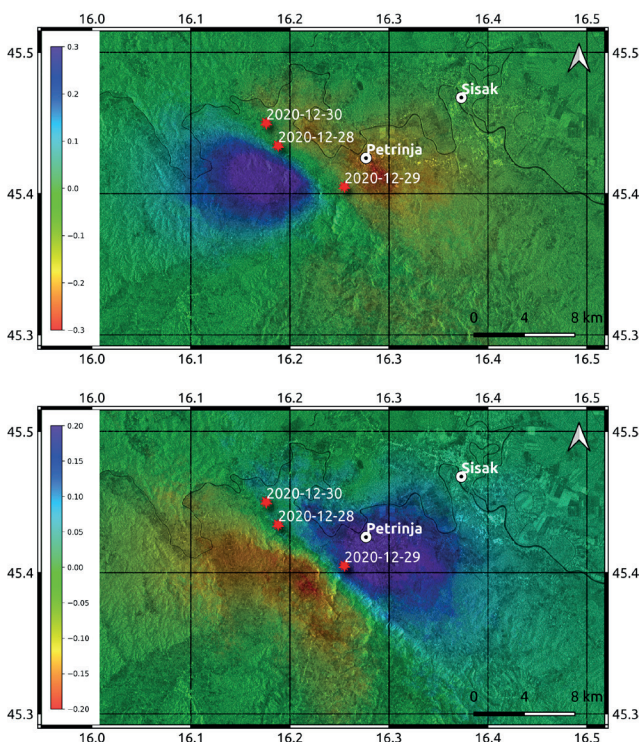


Fig. 4 Line-of-sight displacement fields of 2020.12.28–30. Petrinja Earthquake sequence. Top panel corresponds to the ascending solution, bottom panel to the descending solution

well as in the mountainous area between Slana and Gora (Fig. 4, top panel). Due to the presented LOS deformation field describing the coseismic deformation field along 1D LOS vectors, involving the ascending and descending solution is not adequate to evaluate the 3D deformation vector field. Thus, to perform common interpretation of the two independent observations, constraints or approximations should be applied while determining the corresponding surface deformation [10, 11, 21, 31].

3 Results

The evaluation of the 3D deformation field should include at least three independent sources, and possibly orthogonal observations, to properly construct the geodetic surface deformation expressed in a local East/North/Up (ENU) basis [9, 13, 15, 31]. Such evaluation can be generalized as an ordinary least-squares problem (OLS), as well as weighted least squares problem (WLS), if an a priori estimate of the data is also available. The optimization problem can be characterized with the observation vector that contains the LOS displacement measurements, with a design matrix that includes the look-angle vectors (LOS) of the measurements, as well as the model vector that describes the unknown parameters of 3D deformation components [9, 13, 15, 31]. Obtaining two independent DInSAR derived LOS deformation fields is not adequate to solve such optimization problem and derive the corresponding 3D deformation components, namely the East-West, North-South and Up-Down components.

Regarding the quasi-polar orbits and right-looking acquisition mode of the Sentinel-1 mission, both ascending and descending SAR measurements are sensitive to displacements caused or dominated by the East-West (E-W) deformation component and vertical Up-Down (U-D) component. The accuracy of the measured motions along the North-South axis is significantly lower, than the E-W and U-D components [9, 13, 15, 31]. According to such imaging characteristics, an approximation that the North deformation component has no contribution has been assumed. This approximation leads to the truncated version of the previously discussed OLS and WLS approaches, where a linear system of equations may be solved for the unknown East-West and Up-Down deformation components without redundancy, as presented in [9] and [31]. Different forms of such constrains are commonly described as 2.5D DInSAR analysis, resulting in the East-West and Up-Down deformation component [9, 10, 12, 31]. Applying 2.5D analysis, the common

interpretation of the ascending and descending LOS displacement field of the Petrinja Earthquake sequence has been realized. The results of the East–West component are illustrated in the top-panel of Fig. 5, and the corresponding Up–Down component in the bottom panel of Fig. 5. In order to achieve the common interpretation, both A146 and D124 LOS solutions have been interpreted for the same spatial reference point (SRP_{WGS84}: 45.636395° N, 16.366268° E), which is assumed to be stable.

4 Discussion

As the top panel of Fig. 5 illustrates, significant East–West horizontal displacement occurred along the M6.4 mainshock due to strike slip faulting. The maximum local horizontal displacement towards East, of approximately 43 cm, occurred in the town of Petrinja (Fig. 5, top panel, colormap: blue). Corresponding 45 cm maximum local horizontal displacement towards West occurred in the Slana – Glinska Poljana – Gora – Medurace region (Fig. 5, top panel, colormap: red), ~9 km West of the town of Petrinja. The corresponding Up–Down deformation occurred with a local maximum between the Slana – Glinska Poljana – Gora – Medurace surrounded mountainous area with an approximate local maximum uplift of 19 cm, as the bottom

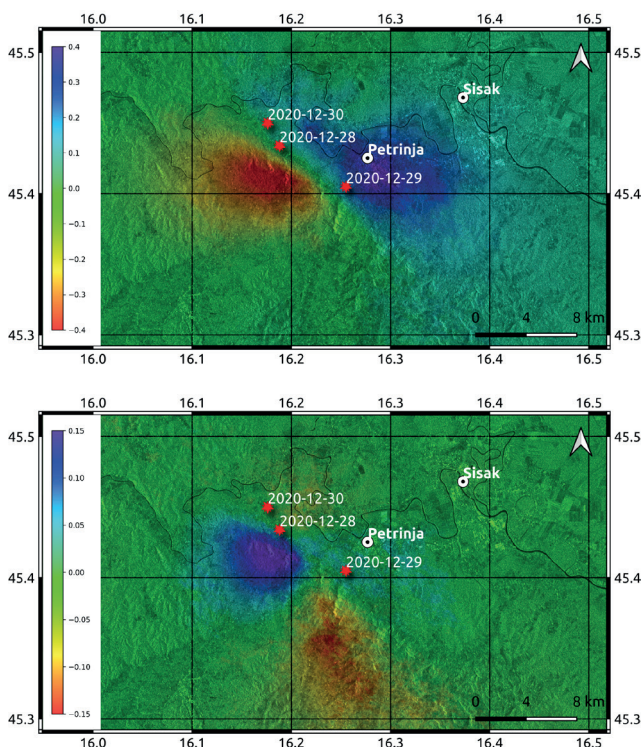


Fig. 5 Results of the 2.5D DInSAR analysis: East–West component (top panel) and Up–Down component (bottom panel) of the 2020.12.28–30. Petrinja Earthquake sequence

panel of Fig. 5 illustrates. The local minimum of the vertical subsidence is 15 cm, the corresponding Up–Down component occurred ~10 km South to Petrinja in the Strasnik–Pecki–Luscani–Donja Bacuga region (Fig. 5, bottom panel, colormap: red). The spatial distribution of the deformations that imply uplift (Fig. 5, bottom panel, colormap: blue), as well as the westward oriented horizontal deformations of the East–West component (Fig. 5, top panel, colormap: red) are spatially well correlated in the Slana – Glinska Poljana – Gora – Medurace area. While the M5.2 foreshock and the M4.8 aftershock can be characterized as oblique dip slip faulting, the M6.4 mainshock clearly derived by strike slip faulting, which led to the significant local horizontal East–West deformations around Petrinja. Furthermore, the Up–Down component indicates the strike-slip faulting and the corresponding FMS related (Fig. 5, bottom panel) quadrupolar, t-cross-pattern feature [32, 33].

5 Conclusions

2.5D differential interferometric analysis was performed for the Petrinja Earthquake Sequence that occurred between 2020.12.28–30., in order to reveal the East–West and Up–Down components of the coseismic deformation. Through presenting the characteristics of the Petrinja Earthquake Sequence, specifying the input data, and presenting the applied data processing methodology, the coseismic horizontal (E–W) and vertical deformation field has been evaluated. The derived coseismic deformation of the strike slip fault can be characterized by a maximum of 45 cm in local horizontal displacements, near Petrinja and in the area of Slana – Glinska Poljana – Gora – Medurace area, 9 km West of Petrinja. The corresponding maximum uplift occurred with +19 cm local displacement near the Slana – Glinska Poljana – Gora – Medurace area. This pattern also shows spatial correlation with the local westward horizontal displacements. The maximum of the subsidence occurred South to Petrinja with an approximated vertical displacement of –15 cm. As the solution derived from the 2.5D differential interferometric indicates, the main coseismic deformation field is restricted to the epicenter of the M6.4 mainshock of the strike slip fault within a radius of 12 km, including the town of Petrinja. Considering the characteristics of the DInSAR technology, the accuracy of displacement measurements along the North–South axis (N–S def. Component) is significantly lower than the presented East–West and Up–Down components. Thus, to retrieve a true 3D deformation field, additional measurements shall be included. Such measurements could include

offset tracking solutions [9, 13, 30, 34, 35], which provide the range and azimuth dependent deformations, resulting in an over-determined OLS/WLS to be solved for the 3D deformation field in ENU basis. Furthermore, by involving multi-temporal INSAR analysis, Atmospheric Phase Screen (APS) estimation can be also realized and compensated. Besides, integrating GNSS data [36] and derived tropospheric models [37, 38] into the InSAR analysis can also aim the precise estimation of APS, as well as the deformation related phase terms. This study provides the coseismic quasi horizontal and vertical components of the Petrinja Earthquake Sequence, which also demonstrates the capabilities of the applied technology for civil engineering purposes, like scopes as deformation hazard mapping and infrastructure monitoring as well.

References

- [1] Bada, G., Grenerczy, G., Tóth, L., Horváth, F., Stein, S., Cloetingh, S., Windhoffer, G., Fodor, L., Pinter, N., Fejes, I. "Motion of Adria and ongoing inversion of the Pannonian Basin: Seismicity, GPS velocities, and stress transfer", In: Stein, S., Mazzotti, S. (eds.) *Continental Intraplate Earthquakes: Science, Hazard, and Policy Issues*, Geological Society of America, Special Papers, 425, 2007, pp. 243–262.
[https://doi.org/10.1130/2007.2425\(16\)](https://doi.org/10.1130/2007.2425(16))
- [2] Devoti, R., D'Agostino, N., Serpelloni, E., Pietrantonio, G., Riguzzi, F., ..., Anzidei, M. "A Combined Velocity Field of the Mediterranean Region", *Annals of Geophysics*, 60(2), S0215, 2017.
<https://doi.org/10.4401/ag-7059>
- [3] Faccenna, C., Becker, T. W., Auer, L., Billi, A., Boschi, L., ..., Serpelloni, E. "Mantle dynamics in the Mediterranean", *Reviews of Geophysics*, 52(3), pp. 283–332, 2014.
<https://doi.org/10.1002/2013RG000444>
- [4] Handy, M. R., Ustaszewski, K., Kissling, E. "Reconstructing the Alps–Carpathians–Dinarides as a key to understanding switches in subduction polarity, slab gaps and surface motion", *International Journal of Earth Sciences*, 104, pp. 1–26, 2015.
<https://doi.org/10.1007/s00531-014-1060-3>
- [5] Grenerczy, G., Kenyeres, A., Fejes, I. "Present crustal movement and strain distribution in Central Europe inferred from GPS measurements", *Journal of Geophysical Research*, 105(B9), pp. 21835–21846, 2000.
<https://doi.org/10.1029/2000JB900127>
- [6] Horváth, F. "Towards a mechanical model for the formation of the Pannonian Basin", *Tectonophysics*, 226, pp. 333–357, 1993.
[https://doi.org/10.1016/0040-1951\(93\)90126-5](https://doi.org/10.1016/0040-1951(93)90126-5)
- [7] Horváth, F., Bada, G., Szafián, P., Tari, G., Ádám, A., Cloetingh, S. "Formation and deformation of the Pannonian Basin: constraints from observational data", *Geological Society London Memoirs*, 32, pp. 191–206, 2006.
<https://doi.org/10.1144/GSL.MEM.2006.032>
- [8] U.S. Geological Survey "Earthquake Lists, Maps, and Statistics", [online] Available at: <https://www.usgs.gov/natural-hazards/earthquake-hazards/lists-maps-and-statistics> [Accessed: 4 January 2021]
- [9] Merryman Boncori, J. P. "Measuring Coseismic Deformation With Spaceborne Synthetic Aperture Radar: A Review", *Frontiers in Earth Science*, 7(16), pp. 1–20, 2019.
<https://doi.org/10.3389/feart.2019.00016>
- [10] Fujiwara, S., Nishimura, T., Murakami, M., Nakagawa, H., Tobita, M., Rosen, P. A. "2.5-D surface deformation of M6.1 earthquake near Mt Iwate detected by SAR interferometry", *Geophysical Research Letters*, 27(14), pp. 2049–2052, 2000.
<https://doi.org/10.1029/1999GL011291>
- [11] Manzo, M., Ricciardi, G. P., Casu, F., Ventura, G., Zeni, G., Borgstöm, S., Berardino, P., Del Gaudio, C., Lanari, R. "Surface deformation analysis in the Ischia Island (Italy) based on spaceborne radar interferometry", *Journal of Volcanology and Geothermal Research*, 151, pp. 399–416, 2006.
<https://doi.org/10.1016/j.jvolgeores.2005.09.010>
- [12] Sato, H. P., Une, H. "Detection of the 2015 Gorkha earthquake-induced landslide surface deformation in Kathmandu using InSAR images from PALSAR-2 data", *Planets and Space*, 68, 47, 2016.
<https://doi.org/10.1186/s40623-016-0425-1>
- [13] Pepe, A., Caló, F. "A Review of Interferometric Synthetic Aperture RADAR (InSAR) Multi-Track Approaches for the Retrieval of Earth's Surface Displacements", *Applied Sciences*, 7(12), 1264, 2017.
<https://doi.org/10.3390/app7121264>
- [14] Earth Resources Observation and Science (EROS) Center "Shuttle Radar Topography Mission (SRTM) 1 Arc-Second Global", USGS.
<https://doi.org/10.5066/F7PR7TFT>
- [15] Wegnüller, U., Werner, C., Strozzi, T., Wiesmann, A., Frey, O., Santoro, M. "Sentinel-1 Support in the GAMMA Software", *Procedia Computer Science*, 100, pp. 1305–1312, 2016.
<https://doi.org/10.1016/j.procs.2016.09.246>

Acknowledgment

The Sentinel-1 data are provided through the Copernicus Program of the European Union and accessed via the Alaska Satellite Facility Distributed Active Archive Center. Corresponding POD Restituted Orbit files were provided by the Sentinel-1 Quality Center. The Digital Elevation Model was retrieved from the SRTM Archive of Earthdata platform supported by the National Aeronautics and Space Administration (NASA). Figures are published via the open source QGIS 3.12 software. DInSAR analysis was conducted with the GAMMA RS Software, under license agreement of Lechner Nonprofit Ltd. Prepared with the professional support of the Doctoral Student Scholarship Program of the Co-operative Doctoral Program of the Ministry for Innovation and Technology from the source of the National Research, Development, and Innovation Fund. The author declares no conflict of interests.

- [16] ESA "Sentinel-1 Product and Algorithms [S1PRD]" [online] Available at: <https://sentinel.esa.int/web/sentinel/technical-guides/sentinel-1-sar/products-algorithms>
- [17] Yague-Martinez, N., Prats-Iraola, R., Gonzalez, F.R., Brcic, R., Shau, R., Geudtner, D., Eineder, M., Bamler, R. "Interferometric Processing of Sentinel-1 TOPS Data", *IEEE Transactions on Geoscience and Remote Sensing*, 54(4), pp. 2220–2234, 2016. <https://doi.org/10.1109/TGRS.2015.2497902>
- [18] Alaska Satellite Facility DAAC "Sentinel-1" [online] Available at: <https://asf.alaska.edu/data-sets/sar-data-sets/sentinel-1/>
- [19] GMV "Sentinels POD Product Handbook" [pdf] 2020. [S1POD] Available at: <https://sentinel.esa.int/documents/247904/3372484/Sentinels-POD-Product-Handbook.pdf>
- [20] Schubert, A., Small, D., Miranda, N., Geudtner, D., Meier, E. "Sentinel-1A Product Geolocation Accuracy: Commissioning Phase Results", *Remote Sensing*, 7, pp. 9431–9449, 2015. <https://doi.org/10.3390/rs70709431>
- [21] Frey, O., Santoro, M., Werner, C. L., Wegmüller, U. "DEM-based SAR pixel-area estimation for enhanced geocoding refinement and radiometric normalization", *IEEE Geoscience and Remote Sensing Letters*, 10, pp. 48–52, 2012. <https://doi.org/10.1109/LGRS.2012.2192093>
- [22] Scheiber, R., Moreira, A. "Coregistration of Interferometric SAR Images Using Spectral Diversity", *IEEE Transactions on Geoscience and Remote Sensing*, 38(5), pp: 2179–2191, 2000. <https://doi.org/10.1109/36.868876>
- [23] Goldstein, R. M., Werner, C. L. "Radar interferogram filtering for geophysical applications", *Geophysical Research Letters*, 25(21), pp. 4035–4038, 1998. <https://doi.org/10.1029/1998GL900033>
- [24] Hanssen, R. F., Teunissen, P. J. G., Joosten, P. "Phase Ambiguity Resolution For Stacked Radar Interferometric Data", In: *Proceedings of the International Symposium on Kinematic Systems in Geodesy, Geomatics and Navigation*, Banff, Canada, 2001, pp. 317–320.
- [25] Paláncz, B., Völgyesi, L. "A Numeric-Symbolic Solution of GNSS Phase Ambiguity", *Periodica Polytechnica Civil Engineering*, 64(1), pp. 223–230, 2020. <https://doi.org/10.3311/PPci.15092>
- [26] Costantini, M. "A novel phase unwrapping method based on network programming", *IEEE Transactions on Geoscience and Remote Sensing*, 36(3), pp. 813–821, 1998. <https://doi.org/10.1109/36.673674>
- [27] Esch, C., Köhler, J., Gutjahr, K., Schuh, W.-D. "On the Analysis of the Phase Unwrapping Process in a D-InSAR Stack with Special Focus on the Estimation of a Motion Model", *Remote Sensing*, 11(19), 2295, 2017. <https://doi.org/10.3390/rs11192295>
- [28] Goldstein, R. M., Zebker, H. A., Werner, C. L. "Satellite radar interferometry: two-dimensional phase unwrapping", *Radio Science*, 23(4), pp. 713–720, 1988. <https://doi.org/10.1029/RS023i004p00713>
- [29] Werner, C. L., Wegmüller, U., Strozzi, T. "Processing strategies for phase unwrapping for INSAR applications", presented at EUSAR Conference, Cologne, Germany, June, 4–6, 2002
- [30] Fernandez, J., Prieto, J.F., Escayo, J., Camacho, A. G., Luzón, F., ..., Mallorquí, J. J. "Modeling the two- and three-dimensional displacement field in Lorca, Spain, subsidence and the global implications", *Scientific Reports*, 8, 14782, 2018. <https://doi.org/10.1038/s41598-018-33128-0>
- [31] Fuhrmann, T., Garthwaite, M. C. "Resolving Three-Dimensional Surface Motion with InSAR: Constraints from Multi-Geometry Data Fusion", *Remote Sensing*, 11(3), 241, 2019. <https://doi.org/10.3390/rs11030241>
- [32] Biggs, J., Bergman, E., Emmerson, B., Funning, G. J., Jackson, J., Parsons, B., Wright, T. J. "Fault identification for buried strike-slip earthquakes using InSAR: The 1994 and 2004 Al Hoceima, Morocco earthquakes", *Geophysical Journal International*, 166, pp. 1347–1362, 2007. <https://doi.org/10.1111/j.1365-246X.2006.03071.x>
- [33] Han, S.-C., Riva, R., Sauber, J., Okal, E. "Source parameter inversion for recent great earthquakes from decade-long observation of global gravity fields", *Journal of Geophysical Research: Solid Earth*, 118(3), pp. 1240–1267, 2013. <https://doi.org/10.1002/jgrb.50116>
- [34] Strozzi, T., Luckman, A., Murray, T., Wegmüller, U., Werner, L.C. "Glacier motion estimation using SAR offset-tracking procedures", *IEEE Transactions on Geoscience and Remote Sensing*, 40(11), pp. 2384–2391, 2002. <https://doi.org/10.1109/TGRS.2002.805079>
- [35] Wang, T., Jónsson, S. "Improved SAR amplitude image offset measurements for deriving three-dimensional coseismic displacements", *IEEE Journal of Selected Topics in Applied Earth Observations and Remote Sensing*, 8(7), pp. 3271–3278, 2015. <https://doi.org/10.1109/JSTARS.2014.2387865>
- [36] Simonetto, E., Durand, S., Burdack, J., Polidori, L., Morel, L., Nicolas-Duroy, J. "Combination of INSAR and GNSS measurements for ground displacement monitoring", *Procedia Technology*, 16, pp. 192–198, 2014. <https://doi.org/10.1016/j.protcy.2014.10.083>
- [37] Juni, I., Rózsa, S. "Validation of a New Model for the Estimation of Residual Tropospheric Delay Error Under Extreme Weather Conditions", *Periodica Polytechnica Civil Engineering*, 63(1), pp. 121–129, 2019. <https://doi.org/10.3311/PPci.12132>
- [38] Rózsa, S. "Modelling Tropospheric Delays Using the Global Surface Meteorological Parameter Model GPT2", *Periodica Polytechnica Civil Engineering*, 58(4), pp. 301–308, 2014. <https://doi.org/10.3311/PPci.7267>

Appendix 1

Summary of SIAB level-1 input data. Including: Relative Orbit Number (RON), interferogram and related role:

S1B_IW_SLC__1SDV_20201224T164933_20201224T165000_024847_02F4D0_7638, RON:A146, 20201224-20201230, MASTER
 S1B_IW_SLC__1SDV_20201224T164958_20201224T165026_024847_02F4D0_C206, RON:A146, 20201224-20201230, MASTER
 S1A_IW_SLC__1SDV_20201230T165014_20201230T165041_035918_0434F0_0C67, RON:A146, 20201224-20201230, SLAVE
 S1A_IW_SLC__1SDV_20201230T165039_20201230T165106_035918_0434F0_DA51, RON:A146, 20201224-20201230, SLAVE
 S1B_IW_SLC__1SDV_20201223T050202_20201223T050228_024825_02F419_7F03, RON:D124, 20201223-20210104, MASTER
 S1B_IW_SLC__1SDV_20210104T050201_20210104T050228_025000_02F9B4_87AE, RON:D124, 20201223-20210104, SLAVE